PPPL-2230 165 7-31-85 J.M.D. (2) I-22147 PPPL-2230

DC20-G

DR. 1175.4

PARABOLIC APPROXIMATION METHOD FOR FAST MAGNETOSONIC WAVE PROPAGATION IN TOKAMAKS

By

C.K. Phillips, F.W. Perkins, and D.W. Hwang

JULY 1985

PLASMA PHYSICS LABORATORY

PPL

DISTRIBUTION OF THIS DOCUMENT IS UNLIMITED

PRINCETON UNIVERSITY

PRINCETON, NEW JERSEY

PREPARED FOR THE U.S. DEPARTMENT OF ENERGY,
UNDER CONTRACT DE-AC02-76-CHO-3073.

PARABOLIC APPROXIMATION METHOD FOR FAST MAGNETOSONIC WAVE PROPAGATION IN TOKAMAKS

C.K. Phillips, F.W. Perkins, and D.Q. Hwang

Plasma Physics Laboratory, Princeton University

Princeton, NJ 08544

PPPL--2230

DE85 015310

ABSTRACT

Fast magnetosonic wave propagation in a cylindrical tokamak model is studied using a parabolic approximation method in which poloidal variations of the wave field are considered weak in comparison to the radial variations. Diffraction effects, which are ignored by ray tracing methods, are included self-consistently using the parabolic method since continuous representations for the wave electromagnetic fields are computed directly. Numerical results are presented which illustrate the cylindrical convergence of the launched waves into a diffraction-limited focal spot on the cyclotron absorption layer near the magnetic axis for a wide range of plasma confinement parameters.

PACS 52.40.Db; 52.50.Gj

I. INTRODUCTION

Auxiliary plasma heating has become an essential component of tokamak research because fusion temperature plasmas cannot be achieved with ohmic heating alone. Though various methods for delivering power to the plasma have been tested, the one most favored in proposed reactor designs [1-3] is bulk ion heating via fast magnetosonic waves in the ion cyclotron range of frequencies (ICRF). This preference is based in part on recent striking experimental results from several tokamaks, particularly the achievement of central ion temperatures in the 3-5 keV range in PLT under the application of 3 MW of power to the plasma.[4] The ready penetration of these waves to the plasma center combined with a cylindrical convergence of the wavefront due to refraction arising from the variation of the Alfvén speed with the peaked density profile and the antenna geometry results in a favorable, centrally concentrated deposition of the applied heating power. The width of the heating profile is determined by the degree of focussing experienced by the waves during the propagation phase and by diffraction effects which limit the wave intensity at the mode conversion/absorption layers[5,6] in the neighborhood of the magnetic axis. Conventional treatments[7-9] of the propagation region utilize ray tracing techniques[10] to solve for the wave electric field and polarization. Since these techniques treat the wave field as a set of discrete, noninteracting wave packets, diffractive and wave interference effects are neglected. Furthermore, the discretization process itself may induce nonphysical, spatially localized fluctuations in power deposition profiles derived using the field solutions in quasilinear damping calculations.[8] Finally, all of these techniques are based on WKB approximations which fail near the absorption/conversion layer due to fine scale structure in the refractive index of the plasma. As a result, mode

converted and transmitted waves, both of which may contribute significantly to the heating process, are ignored by these methods. A connection between fast wave propagation solutions and solutions to the full wave equation in the absorption/mode conversion layer[11,12] is needed.

To address this issue, we have developed a new algorithm which is capable of computing continuous representations for the fast magnetosonic wave electric field in a model tokamak equilibrium consisting of circular, concentric flux surfaces. The plasma cross section is divided into three regions as indicated in Fig. 1. Propagation in Region I is influenced primarily by the radial variation of the density. Though variations arising from the toroidal nature of the equilibrium could also be important, we will not assess those effects in the current study. A parabolic approximation[13-15] of the fast wave equation in the cold plasma limit is utilized to treat Region I, which extends from the plasma edge to a transition layer near the magnetic axis of the equilibrium. This approximation has been used previously to study vacuum focussing of laser beams,[15] acoustic wave propagation in oceans,[16] propagation of beamed signals through optical fibers and other inhomogeneous media,[17] and propagation of the high frequency extraordinary mode in a uniformly magnetized, inhomogeneous plasma slab.[18] By using this approximation, we are able to solve directly for the wave amplitude, thereby retaining the diffractive and wave interference effects which are ignored by ray tracing methods.

Region II consists of a transition layer in which diffraction limits the extent of the focussing of the incident wavefront. As a first approximation in this region, we neglect effects related to density and magnetic field variations in comparison to the diffractive effects and treat the propagation using a uniformly magnetized, homogeneous, cold plasma slab model. Fast

Fourier Transforms provide the connection between the paraxial representations obtained in Region I and the full field solutions obtained in the transition layer. Ion cyclotron absorption and mode conversion effects have a pronounced influence on the wave physics in Region III. Detailed analyses of the wave fields in the absorption/mode conversion layer have been derived by others[11,12] by solving the linearized Vlasov-Maxwell equations in slab geometry with one-dimensional equilibrium magnetic field gradients. An advantage to our approach is that the two-dimensional cold plasma propagation solutions we generate in Regions I and II may be readily coupled via FFT's to the fully kinetic one-dimensional solutions provided by mode conversion theory in Region III in a manner which properly accounts for the coherence of the incident wavefront parallel to the absorption layer. In this manner, power deposition profiles can be obtained which naturally couple the wave propagation characteristics in Regions I and II with the absorption and mode conversion effects which dominate Region III.

In this paper, a derivation of the equations governing fast magnetosonic wave propagation in tokamaks will be presented along with the corresponding numerical results. The coupling of these calculations to one-dimensional kinetic solutions for the fields in the absorption/conversion layer of Region III is left for future studies. A derivation of the parabolic wave equation appropriate for fast magnetosonic wave propagation in tokamaks is presented in Sec. II along with a discussion of the approximations used. The transition layer is discussed in Sec. III, while results from the numerical code are given in Sec. IV. Conclusions and discussion of future applications are summarized in the final section.

II. DERIVATION OF PARABOLIC WAVE EQUATION

In a tokamak discharge, propagation of the fast magnetosonic wave between the periphery of the plasma and the plasma core is dominated by refraction arising from radial gradients in the plasma density. Referring to Fig. 1, in Region I the wave is assumed to propagate primarily in the radial direction with a slow amplitude modulation induced by weak gradients in the equilibrium over a radial wavelength. Poloidal variations, which are proportional to $1/r\ \partial/\partial\theta$, are taken to be much weaker than the radial variations which are proportional to $\partial/\partial r$. Thus, for a reactor-sized plasma, one finds that $k_\perp \sim k_r >> k_\theta, k_\eta$, where $r, \perp, \theta, \eta$ denote the radial, perpendicular, poloidal, and parallel directions, and k_i denotes the i^{th} component of the wave vector. Furthermore, the equilibrium gradient scale lengths tend to be much longer than the radial wavelength over much of the discharge. For more moderately sized tokamaks such as PLT the radial wavelength can approach the size of the minor radius. Nevertheless, as will be demonstrated in Sec. IV, adequate representations for the wave electric fields in the propagation region may still be obtained with the assumption that $\delta \sim 1/k_\perp a << 1$, where a is the minor radius of the discharge. These two orderings, that $k_r >> k_\theta, k_\eta$ and that $\delta << 1$, form the physical basis for the parabolic or small angle propagation, approximation.

We therefore consider a simplified model of a tokamak in which focussing by radial gradients is retained but complexities arising from the toroidal nature of the equilibrium are ignored. The plasma is assumed to be a poloidally and axially symmetric cylindrical column with a radially varying density profile and concentric flux surfaces. A model density profile is chosen which reasonably represents experimentally observed profiles while providing mathematical tractability and computational efficiency for the wave

propagation calculations. The chosen density profile, displayed in Fig. 2, has the form:

$$n = \begin{cases} n_o & o \leq r \leq \frac{a}{2} \\ n_o \left[1 - \left(\frac{2r-a}{a}\right)^2\right] & \frac{a}{2} \leq r \leq a \end{cases} \qquad (1)$$

where n_o is the density on axis. The central region of the tokamak is assumed to have a constant density. More general profile shapes can readily be incorporated into our numerical code. The magnetic field considered consists of a strong, uniform axial component, B_T, and a weak, radially inhomogeneous poloidal component, B_p, such that

$$\bar{B} = B_p(r)\hat{\theta} + B_T\hat{z} \ , \qquad (2)$$

where $B_p/B_T \sim O(\varepsilon) << 1$, and $\hat{\theta}$, $\hat{z}$ are unit vectors in the poloidal and axial directions, respectively. Toroidal effects are not included. Though we initially retain the effects of rotational transform and shear, it will be shown that these terms have a negligible effect on the wave propagation in a low beta, large aspect ratio tokamak.

Dielectric properties of the plasma medium are modelled with the cold plasma dielectric tensor[19] denoted by:

$$\overline{\overline{\varepsilon}} = \begin{bmatrix} \varepsilon_\perp & i\varepsilon_x & 0 \\ -i\varepsilon_x & \varepsilon_\perp & 0 \\ 0 & 0 & \varepsilon_\parallel \end{bmatrix} \qquad (3)$$

where

$$\varepsilon_\perp = 1 + \sum_i \frac{\omega_{pi}^2}{\Omega_i^2} \frac{1}{1 - \omega^2/\Omega_i^2} \ , \qquad (4)$$

$$\varepsilon_x = \sum_i \frac{\omega_{pi}^2}{\Omega_i^2} \frac{\sigma_i \Omega_i}{\omega} \frac{1}{1 - \omega^2/\Omega_i^2} , \tag{5}$$

$$\varepsilon_\parallel = 1 - \sum_i \frac{\omega_{pi}^2}{\omega^2} . \tag{6}$$

In Eqs. (3-6), the plasma frequency, ω_{pi}, for the i^{th} species is defined by

$$\omega_{pi}^2 = \frac{4\pi n_i Z_i^2 e^2}{m_i} , \tag{7}$$

the cyclotron frequency of the i^{th} species is given by

$$\Omega_i = \frac{Z_i eB}{m_i c} , \tag{8}$$

ω is the wave frequency, σ_i is the sign of the charge of the i^{th} species, e is the charge of a proton, and m_i is the mass of the i^{th} species. This tensor has been defined relative to the local magnetic field frame, $\hat{r}$, $\hat{\eta}$, $\hat{b}$, where $\hat{r}$ is a radial unit vector, $\hat{b}$ is a unit vector parallel to the total equilibrium magnetic field, and $\hat{\eta} = \hat{b} \times \hat{r}$. The rotation matrix from the cylindrical frame to the local frame is given by $\overline{\overline{R}}$, where

$$\overline{\overline{R}} = \begin{bmatrix} 1 & 0 & 0 \\ 0 & b_T & -b_p \\ 0 & b_p & b_T \end{bmatrix} , \tag{9}$$

with $b_p = B_p/B$ and $b_T = B_T/B$.

The starting point for the analysis is the Maxwell equations for a cold plasma dielectric medium in the usual fast wave limit, i.e., the parallel electric field, $E_\parallel$, given by

$$E_{\parallel} = b_p E_\theta + b_T E_z \tag{10}$$

is assumed to vanish in the limit $m_e/m_i \to 0$. By assuming a harmonic time dependence at a frequency ω, and Fourier analyzing in the axial direction of symmetry, the wave equation may be written in the form:

$$\nabla \times \nabla \times \bar{E} = \frac{\omega^2}{c^2} \bar{\bar{\varepsilon}} \cdot \bar{E} \, . \tag{11}$$

Upon transforming from the cylindrical frame to the local frame using the rotation matrix, $\bar{\bar{R}}$, the components of Eq. (11) which govern the radial electric field, E_r, and the poloidal electric field, E_θ, may be written as:

$$\gamma_1 E_r - \frac{1}{r^2}\frac{\partial^2 E_r}{\partial \theta^2} + \frac{i}{r}\frac{\partial}{\partial \theta}\frac{1}{r}\frac{\partial}{\partial r}(rE_\theta) - \frac{ik_z}{b_T}\frac{\partial}{\partial r}(b_p E_\theta) - i\gamma_2 \frac{E_\theta}{b_T} = 0 \tag{12}$$

and

$$\left[\gamma_1 - k_z^2 b_p^2\right] E_\theta - b_T^2 \frac{\partial}{\partial r}\frac{1}{r}\frac{\partial}{\partial r}(rE_\theta) + b_T^2 \frac{\partial}{\partial r}\frac{1}{r}\frac{\partial E_r}{\partial \theta} + i\gamma_2 b_T E_r$$

$$- \frac{2ik_z b_p b_T}{r}\frac{\partial E_\theta}{\partial \theta} - \frac{ik_z b_p b_T}{r}\frac{\partial}{\partial r}(rE_r) - \frac{b_p}{r}\frac{\partial}{\partial r} r \frac{\partial}{\partial r}(b_p E_\theta) - \frac{b_p^2}{r^2}\frac{\partial^2 E_\theta}{\partial \theta^2} = 0 \tag{13}$$

where

$$\gamma_1 = k_z^2 - (\omega^2/c^2)\,\varepsilon_\perp , \tag{14}$$

$$\gamma_2 = \omega^2/c^2\ \varepsilon_x,$$

and k_z is the component of the wave vector in the $\hat{z}$ direction.

Based on the assumption that poloidal variations of the wave field are much weaker than the radial variations, Eqs. (12) and (13) may be approximated by treating poloidal derivatives as small perturbations and retaining only terms through order $\partial^2/\partial\theta^2$. Solving Eq. (12) iteratively yields an algebraic equation for the poloidal electric field in the form:

$$E_r = \frac{i\gamma_2}{\gamma_1 b_T} E_\theta - \frac{1}{\gamma_1 r^2} \frac{\partial}{\partial\theta} \frac{\partial}{\partial r} (rE_\theta) + \frac{i\gamma_2}{b_T \gamma_1^2} \frac{1}{r^2} \frac{\partial^2 E_\theta}{\partial\theta^2} + \frac{ik_z}{\gamma_1 b_T} \frac{\partial}{\partial r} (b_p E_\theta)$$
$$+ \frac{ik_z}{\gamma_1^2 b_T} \frac{1}{r^2} \frac{\partial^2}{\partial\theta^2} \frac{\partial}{\partial r} (b_p E_\theta) \quad . \tag{15}$$

Insertion of this expression for E_r into Eq. (13), followed by a modest amount of algebra and discarding of higher order terms, yields a single partial differential equation for the poloidal electric field,

$$\frac{\partial}{\partial r} \frac{1}{r} \frac{\partial}{\partial r} (rE_\theta) + k_o^2(r) E_\theta - \frac{ib_T\gamma_2}{\gamma_1 r} \frac{\partial \ln(\gamma_2/r^2\gamma_1)}{\partial r} \frac{\partial E_\theta}{\partial\theta} + \frac{1}{r^2} \frac{\partial^2 E_\theta}{\partial\theta^2}$$
$$- \frac{2i\ k_z b_p b_T}{r} \frac{\partial E_\theta}{\partial\theta} + \frac{k_z b_p \gamma_2}{\gamma_1} \frac{\partial \ln(r\gamma_2/b_p\gamma_1)}{\partial r} E_\theta - \frac{2i\ k_z b_T b_p k_o^2}{\gamma_1} \frac{\partial E_\theta}{\partial\theta}$$
$$+ \frac{\partial^2}{\partial\theta^2} \left[\left(\frac{1}{r^2\gamma_1}\right)' \frac{1}{r} \frac{\partial}{\partial r} (rE_\theta) \right] + \frac{k_z b_p \gamma_2}{r^2 \gamma_1^2} \frac{\partial \ln(\gamma_2/rb_p\gamma_1^2)}{\partial r} \frac{\partial^2 E_\theta}{\partial\theta^2}$$
$$+ \frac{2ik_z b_T}{r} \left[\left(\frac{b_p}{\gamma_1}\right)' - \frac{b_p}{\gamma_1 r} \right] \frac{\partial^2 E_\theta}{\partial r \partial\theta} - \frac{2k_z b_p b_T^2 \gamma_2}{r^2 \gamma_1^2} \frac{\partial \ln(\gamma_2/r^2\gamma_1)}{\partial r} \frac{\partial^2 E_\theta}{\partial\theta^2}$$
$$+ ik_z b_T \left[\frac{2b_p}{\gamma_1 r^3} + \left(\frac{b_p}{\gamma_1 r}\right)' + \frac{b_p}{r} \left(\frac{1}{\gamma_1 r}\right)' \right] \frac{\partial E_\theta}{\partial\theta} = 0 \tag{16}$$

where primes denote derivatives with respect to radius and where

$$k_o^2(r) = \frac{\gamma_2^2 - \gamma_1^2}{\gamma_1} = \left(\frac{\omega}{c^2}\right)^2 \frac{\varepsilon_x^2 - \left((ck_z/\omega)^2 - \varepsilon_\perp\right)^2}{(ck_z/\omega)^2 - \varepsilon_\perp} . \tag{17}$$

To the extent that $\partial/\partial r \gg 1/r\ \partial/\partial\theta$, $b_p \approx r/qR \ll 1$, $\partial^2/\partial r^2 \sim O(k_o^2)$, and $k_z \ll k_o$, the first two terms in Eq. (16) are dominant and of order $k_o^2 E_\theta$. The next two terms contain the primary diffractive effects and are of order δ^2 relative to the dominant terms, where $\delta \sim 1/k_\perp a\ \partial/\partial\theta$. Lowest order corrections introduced by the rotational transform and shear are contained in the next three terms. Since these contributions are at most of order $\sim k_z/k_o\ 1/\delta$ in comparison to the diffraction terms, they have a weaker effect on the wave propagation and will be ignored in the remainder of this paper. The remaining terms are significant only at the plasma edge, where γ_1 becomes very small, and hence will also be ignored in the wave propagation calculations.

With these considerations, the appropriate equation governing the poloidal electric field can be written as:

$$\frac{\partial}{\partial r}\frac{1}{r}\frac{\partial}{\partial r}(rE_\theta) + k_o^2(r)E_\theta - i\,a(r)\frac{\partial E_\theta}{\partial\theta} + \frac{1}{r^2}\frac{\partial^2 E_\theta}{\partial\theta^2} = 0 \tag{18}$$

where b_T has been set equal to unity with little error introduced, and the coefficient, $a(r)$, is defined as:

$$a(r) = \frac{\gamma_2}{r\gamma_1}\frac{\partial \ln(\gamma_2/r^2\gamma_1)}{\partial r} . \tag{19}$$

Similarly, the last two terms in Eq. (15) for E_r may also be neglected, leading to:

$$E_r = \frac{i\gamma_2}{\gamma_1} E_\theta - \frac{1}{\gamma_1 r^2} \frac{\partial}{\partial \theta} \frac{\partial}{\partial r} (rE_\theta) + \frac{i\gamma_2}{\gamma_1^2} \frac{1}{r^2} \frac{\partial^2 E_\theta}{\partial \theta^2} \quad . \tag{20}$$

The first two terms in Eq. (18) determine the overall radial structure of the wave, while the remaining smaller terms describe distortions arising from focussing and diffraction. As we will show further on, the third term introduces a poloidal skewing of the wavefront, while the final term causes a poloidal spreading of the width of the wave packet.

The fast radial wavelike dependence, $\varepsilon_o(r)$, can be separated from the more slowly varying amplitude, $\psi(r,\theta)$, of E_θ by substituting

$$E_\theta (r,\theta) = \varepsilon_o(r)\, \psi (r,\theta) \tag{21}$$

into Eq. (18), with the result

$$\psi \left[\frac{\partial}{\partial r} \frac{1}{r} \frac{\partial}{\partial r} (r\varepsilon_o) + k_o^2(r)\, \varepsilon_o \right] + \varepsilon_o \left\{ \left[\frac{2}{r^{1/2}\, \varepsilon_o} \frac{\partial}{\partial r} (r^{1/2} \varepsilon_o) \right] \frac{\partial \psi}{\partial r} \right.$$

$$\left. - i\, a(r) \frac{\partial \psi}{\partial \theta} + \frac{1}{r^2} \frac{\partial^2 \psi}{\partial \theta^2} \right\} = 0 \quad . \tag{22}$$

The waveform $\varepsilon_o(r)$ is determined by a generalized Bessel equation of the form:

$$\frac{\partial}{\partial r} \frac{1}{r} \frac{\partial}{\partial r} (r\varepsilon_o) + k_o^2\, (r)\, \varepsilon_o = 0 \quad . \tag{23}$$

For a homogeneous plasma, k_o^2 is constant and the travelling wave solutions of Eq. (23) reduce to Hankel functions of the first and second kind, representing outward and inward propagating waves, respectively. Hence, the general solution to Eq. (23) will be written as:

$$\varepsilon_o(r) = C_1 \varepsilon_o^{(1)}(r) + C_2 \varepsilon_o^{(2)}(r) \tag{24}$$

where the analogous wavelike solutions to the homogeneous Bessel equation are denoted by $H_1^{(1)}(k_o r)$ and $H_1^{(2)}(k_o r)$, respectively. In this manner, ingoing waves, launched by the antenna or reflected from the conducting wall, and outgoing waves, transmitted through or reflected from the mode conversion/absorption layer, are readily simulated.

The remaining terms in Eq. (22) govern diffractive distortion of the wavefront. Since the amplitude function, ψ, is a slowly varying function of radius relative to the waveform, $\varepsilon_o^{(1)}$, the term $\partial^2\psi/\partial r^2$ has been neglected. This approximation is the key feature of the parabolic method. With this approximation, the equation for the amplitude function has been reduced to a parabolic partial differential equation of the form

$$\frac{\partial \psi^{(i)}}{\partial r} - i\, a(r)\, \phi^{(i)}(r)\, \frac{\partial \psi^{(i)}}{\partial \theta} + \frac{1}{r^2}\, \phi^{(i)}(r)\, \frac{\partial^2 \psi^{(i)}}{\partial \theta^2} = 0 \,. \tag{25}$$

The coefficient, $\phi^{(i)}(r)$, depends on the particular waveform chosen,

$$\phi^{(i)}(r) = \frac{\varepsilon^{(i)}(r)}{2\, \partial \varepsilon^{(i)}(r)/\partial r} \,, \tag{26}$$

where $\varepsilon^{(i)}(r) \equiv r^{1/2} \varepsilon_o^{(i)}(r)$. It is Eq. (25) that is commonly referred to as the parabolic or paraxial approximation of the wave equation.

Solutions of Eq. (25) are readily obtained in the form

$$\psi^{(i)}(r,\theta) = \sum_m \psi_m^{(i)}(r_s^{(i)}) \exp\left\{ im\left(\theta + F_1^{(i)}(r)\right) - im^2 F_2^{(i)}(r) \right\} , \tag{27}$$

where

$$F_1^{(i)}(r) = i\int_{r_s^{(i)}}^{r} dr' \, a(r') \, \phi^{(i)}(r') \tag{28}$$

$$F_2^{(i)}(r) = i\int_{r_s^{(i)}}^{r} dr' \, \frac{\phi^{(i)}(r')}{(r')^2} \tag{29}$$

and where $r_s^{(i)}$ is a conveniently chosen radius for evaluation of constants. The summation is over the poloidal harmonics, m, present in the wave. Physically, $F_1^{(i)}(r)$ represents a poloidal rotation of the wavefront as the wave propagates into or out of the plasma core. To this order, the rotation is directly attributable to the anisotropy of the plasma dielectric properties, as contained in the function a(r). In the limit of short radial wavelengths and flat density profiles, the function $\phi^{(i)}(r)$ asymptotically reduces to $i/2k_o$ for an inward travelling wave and $-i/2k_o$ for an outward travelling wave. Hence, the wavefront rotation proceeds in opposite poloidal directions for an inward vs. outward directed wave and is more pronounced for longer radial wavelengths. Finally, $F_2^{(i)}(r)$ represents diffraction of the wavefront caused by a variation in the relative phasing of the different poloidal harmonics as the wave propagates radially.

Using Eqs. (21), (24), and (27), the general solution for the poloidal electric field in the propagation region becomes:

$$E_\theta(r,\theta) = \sum_{i=1}^{2} c_i \varepsilon_o^{(i)}(r) \sum_m \psi_m^{(i)}\left(r_s^{(i)}\right) \exp\left\{im\left(\theta + F_1^{(i)}(r)\right) - im^2 F_2^{(i)}(r)\right\} . \tag{30}$$

Through an appropriate choice of the constants c_i and $\psi_m^{(i)}(r_s^{(i)})$, waves launched from an antenna, reflected from the conducting wall of the vacuum vessel, and transmitted through or reflected from the cyclotron

absorption/mode conversion layer may be computed. Evaluation of these constants will be discussed in general and numerical solutions appropriate for the case of single pass absorption will be presented in Sec. IV.

The propagation of the fast wave between the plasma edge and the transition layer is completely described by Eqs. (20), (21), (23), and (25). Solutions of these equations provide a continuous representation of the wave electric fields that correctly account for the dominant refractive and diffractive effects. The key approximations utilized include the slow poloidal variations of the wave field relative to the radial variations, and the factorization of the poloidal electric field into a rapidly convergent cylindrical waveform modulated by a more slowly varying amplitude function. In this manner, diffractive effects are isolated in the amplitude function. The connection of the propagation solutions to those appropriate within the transition layer will be discussed in the next section.

III. THE TRANSITION LAYER

As the fast magnetosonic wave propagates from the edge of the plasma towards the plasma core, it enters a transition layer in which the wavefront has become so strongly focussed in the poloidal direction, that a full two-dimensional treatment of the wave fields is required. The transition layer is indicated by Region II in Fig. 1. Since the wave intensity in this layer has been focussed primarily into the constant density regions near the magnetic axis, the density will be approximated by its central value, n_c, throughout the entire layer. Furthermore, since this region is outside of the mode conversion/cyclotron absorption layer, kinetic effects may be neglected and a cold plasma model may be assumed. With these approximations, the final focussing of the fast wave in this region into a diffraction-limited focal

spot on the absorption layer may be described using a homogeneous, uniformly magnetized plasma slab.

In Cartesian coordinates, the components of the wave equation, Eq. (11), in the fast wave limit are given as:

$$\frac{\partial^2 E_y}{\partial x \partial y} - \frac{\partial^2 E_x}{\partial y^2} + \gamma_1 E_x - i\gamma_2 E_y = 0 \tag{31}$$

$$\frac{\partial^2 E_x}{\partial x \partial y} - \frac{\partial^2 E_y}{\partial x^2} + \gamma_1 E_y + i\gamma_2 E_x = 0 \tag{32}$$

where $\hat{x}$ is directed outward along the major radial direction and $\hat{y}$ is directed upward perpendicular to the midplane of the tokamak. The y-dependence of the fields is represented using Fast Fourier Transforms (FFT):

$$E_i(x,y) = \sum_{n=-N/2}^{N/2-1} E_i(x,k_n) e^{ik_n y} \tag{33}$$

where $i = x,y$ and $k_n = n\Delta k$. For a slab of height $2L$, the minimum number of harmonics, N, needed to resolve accurately a structure with a typical wavenumber, k_o, is approximately equal to $2k_oL/\pi$. The corresponding mode spacing, Δk, is equal to π/L. Fast Fourier Transform algorithms operate most efficiently when N is rounded upwards to a suitable value of 2^p, where p is a positive integer. Inserting Eq. (33) into Eqs. (31-32) and adopting the notation $E_{i,k_n} \equiv E_i(x,k_n)$, leads to an algebraic equation for E_{x,k_n} in the form:

$$E_{x,k_n} = \frac{i\gamma_2 E_{y,k_n} - ik_n \dfrac{\partial E_{y,k_n}}{\partial x}}{\gamma_1 + k_n^2} \tag{34}$$

and a simple plane wave equation for E_{y,k_n}:

$$\frac{\partial^2 E_{y,k_n}}{\partial x^2} + (k_o^2 - k_n^2)\, E_{y,k_n} = 0 \ . \tag{35}$$

By using the linearly independent solutions of Eq. (35) in Eq. (33), the general solution for $E_y(x,y)$ in the transition layer consists of a sum of waves travelling in the $\pm$ x directions:

$$E_y(x,y) = \sum_{n=-N/2}^{N/2-1} e^{ik_n y} \left\{ d_n^{(1)} \exp\left[i\,(k_o^2 - k_n^2)^{1/2} \left(x - x_s^{(1)}\right)\right] \right.$$

$$\left. + d_n^{(2)} \exp\left[-i\,(k_n^2 - k_o^2)^{1/2} \left(x - x_s^{(2)}\right)\right]\right\} \tag{36}$$

where the mode amplitudes, $d_n^{(i)}$, are evaluated at $x = x_s^{(i)}$. For the special case of $k_o^2 = k_n^2$, the modes corresponding to $d_n^{(1)}$ and $d_n^{(2)}$ coalesce into a single constant solution and a second linearly independent solution corresponding to a field amplitude that grows linearly with x. As will be discussed in the next section, waves which are incident upon, reflected from, or transmitted through the adjacent absorption layer are readily simulated with a proper choice of the coefficients, $d_n^{(i)}$.

IV. NUMERICAL RESULTS

By utilizing the solutions for the wave electric fields developed in the preceding two sections, we have developed an algorithm which computes the propagation of fast magnetosonic waves between the launching structure at the plasma periphery and the cyclotron absorption/mode conversion layer in the core. In general, the method is numerically efficient since for a given value of $k_\parallel$, only six radial integrations are required to generate the waveforms $\varepsilon_o^{(i)}(r)$ and the associated phase functions $F_1^{(i)}(r)$, $F_2^{(i)}(r)$ for $i = 1,2$, as

defined in Eqs. (24, 28, 29). The remainder of the code is devoted to the evaluation of the various constants and functions indicated in Eqs. (30, 36). By way of contrast, in a ray tracing simulation of the wave propagation, the minimum number of integrations required is at least equal to the total number of rays required to represent accurately the poloidal spectrum of the launched wave.

In the case of strong single pass absorption, the evaluation of the constants in the propagation regions is straightforward. Beginning in Region I, the solution consists of an incoming wave launched at $r = r_o$ by an antenna located on the low field edge of the discharge. In principle, r_o is somewhat less than the minor radius of the plasma due to the presence of a thin evanescent layer at the plasma edge. In practice, the width of this layer is sufficiently thin for fixed values of $k_\parallel \ll k_\perp$ so its presence may be ignored. To demonstrate this, consider Eq. (18) near the plasma edge in a slab model limit in which poloidal variations and cylindrical geometry effects have been ignored. Assuming a linear variation of k_o^2 with r and specializing to the case of minority hydrogen heating in a deuterium majority plasma, Eq. (18) can be cast into the form:

$$\frac{\partial^2 \varepsilon_o}{\partial r^2} + \frac{4\omega^2}{aV_{A,o}^2}(a-r)\,\varepsilon_o = 0 \tag{37}$$

where $V_{A,o}^2 \equiv B^2/4\pi n_o m_D$, with m_D being the mass of the deuterium ions. By introducing the dimensionless variable

$$u = \frac{(a-r)}{\ell} \tag{38}$$

where

$$\ell^3 = \frac{a\, V_{A,o}^2}{4\omega^2} , \tag{39}$$

Eq. (37) is transformed into an Airy equation:

$$\frac{\partial^2 \varepsilon_o}{\partial u^2} + u\varepsilon_o = 0 . \tag{40}$$

Since the transition from evanescence to propagation takes place in a characteristic distance ℓ which is small compared to other characteristic lengths of the system,

$$\frac{\ell}{a} = \left(\frac{1}{4k_o^2 a^2}\right)^{1/3} << 1, \quad k_z \ell << 1, \quad \frac{\ell}{a}\frac{\partial}{\partial\theta} << 1, \tag{41}$$

we will ignore the evanescent layer in our current model.

Returning to the evaluation of Eq. (30), the amplitude of the outgoing wave, c_1, is set equal to zero while the amplitude, c_2, and poloidal harmonic content, $\psi_m^{(2)}$, of the incoming wave are evaluated at $r_s^{(2)} = a$. To lowest order in the Poynting flux at r=a, the incoming wave amplitude, c_2, associated with an incident power, P_o, is equal to:

$$c_2 = \left\{\frac{8\pi\omega P_o}{c^2 a\left[\mathrm{Real}\left(\iota\, \varepsilon_o^{(2)}\, \partial\varepsilon_o^{(2)*}/\partial r\right) - \gamma_2 |\varepsilon_o^{(2)}|^2/a\gamma_1\right]_{r=a}}\right\}^{1/2} . \tag{42}$$

The Fourier amplitudes, $\psi_m^{(2)}(a)$, are determined from an assumed poloidal structure, $f(\theta)$, of the wave launched by the antenna, such that:

$$E_\theta(a,\theta) = c_2\, \varepsilon_o^{(2)}(a)\, f(\theta) , \tag{43}$$

$$\frac{\iota\omega}{c} B_z(a,\theta) = \left[\frac{1}{r}\frac{\partial}{\partial r}(rE_\theta) - \frac{1}{r}\frac{\partial E_r}{\partial\theta}\right]_{r=a} , \tag{44}$$

$$B_z(a,\theta) = \begin{cases} B_o \cos[\pi/2\ (\theta/\theta)_m] & |\theta| < \theta_m \\ 0 & |\theta| > \theta_m \end{cases} \qquad (45)$$

where 2 x θ_m is equal to the maximum angular extent of the launched wavefront. The function $f(\theta)$ is normalized such that

$$\int_{-\pi}^{\pi} |f(\theta)|^2\, d\theta = 1 \quad . \qquad (46)$$

In Fig. 3, the corresponding current density profile in the launching structure considered in this report is displayed.

Radial and poloidal electric fields evaluated along the interface between Region I and Region II at x = xo determine the coefficients, $d_n^{(2)}$, of the inward propagating wave in the transitional region. Projecting from cylindrical to slab geometry, the coefficients are determined using the relationship:

$$E_y(x_o,y) = E_r[r(x_o,y),\ \theta(x_o,y)]\sin\theta(x_o,y)$$

$$+ E_\theta[r(x_o,y),\ \theta(x_o,y)]\cos\theta(x_o,y). \qquad (47)$$

For the case of strong single pass absorption, there is no wave reflected back from the absorption layer so the Fourier amplitudes, $d_n^{(1)}$, which comprise an outgoing wave in the transition region, all vanish.

Our algorithm is readily adaptable to treat the case of multiple pass absorption. The amplitudes E_{y,k_n} and associated wavenumbers k_n evaluated at $x = x_{co}$ (or x_{c1}) for waves incident from the outside (or inside) of the torus serve as inputs to a linear mode conversion analysis of the cyclotron absorption/mode conversion layer of Region III. A kinetic treatment of the

fields in Region III yields an absorption profile plus amplitudes associated with transmitted, reflected, and mode converted waves. Since the mode converted wave is assumed to damp rapidly via electron Landau damping, its propagation away from the kinetic layer will not be computed in the current model. Amplitudes for the outgoing waves in the bordering transition layers are determined at $x = x_{co}$ or $x = x_{c1}$ from the reflected and transmitted wave amplitudes, respectively. Similarly, the outgoing waves in the transition layers determine the characteristics of outgoing waves in the outer propagation region. Finally, the amplitudes of waves reflected back into the plasma from the conducting wall are determined by the requirement that E_θ vanish on the wall. In this fashion, multiple passes can be computed until all incident power is deposited into the plasma.

The code has been used to simulate fast magnetosonic wave propagation in three different sized tokamaks. We have considered reactor grade plasmas, breakeven type devices such as TFTR or JET, and moderately sized research tokamaks such as PLT. Parameters characterizing minority hydrogen in deuterium majority heating schemes for each of these devices are summarized in Table I. The assumed poloidal structure of the current in the half-turn antenna is the same for each case, with $\theta_m = 80°$. In Fig. 4, the real portion of the incoming waveform, $\varepsilon_o^{(2)}(r)$, is displayed vs. normalized minor radius for each tokamak considered. The relative number of radial wavelengths per minor radius varies significantly between the three cases, due to variations in the relative densities and minor radii. Since the perpendicular index of refraction $n_\perp \sim ck_\perp/\omega$, is proportional to density, focussing effects are expected to be more pronounced in reactor-sized devices than in PLT.

Cylindrical convergence of the launched wave into a focal spot on the absorption layer is illustrated by the contours of the real portion of axial

wave magnetic field given in Figs. 5-7 for each device considered. Single pass absorption has been assumed. Because of the focussing of the launched wavefront, ICRF power deposition should be highly concentrated in the central regions of the discharge. A comparison of the three figures reveals that due to the smaller value of $n_{\parallel}$ in PLT, less focussing of the launched wave occurs, resulting in a relatively wider distribution of incident power on the absorption layer.

By inference from Figs. 5-7, the minimum relative diameter of the focal spot to the plasma diameter decreases as the size and density of the plasma increase. In addition, the anticipated width of the power deposition profile will increase as the location of the cyclotron absorption layer moves away from the magnetic axis of the device where the minimum focal spot diameter occurs. For the cases considered, the relative diameter of the focal spot to the plasma diameter decreases by about a factor of two from PLT to a reactor. Finally, as discussed in Sec. II, poloidal rotation of the incident wavefront is most pronounced for PLT because of the lower operating densities and hence longer radial wavelengths for the fast wave in the device.

As a final example, a contour plot of the real portion of the axial wave magnetic field in a compact ignition device is displayed in Fig. 8. A deuterium-tritium plasma with a 10% hydrogen minority concentration and a central electron density of 4×10^{14} cm^{-3} has been considered. The poloidal extent of the launched wave has been limited to $\pm$ 30° to model the fields radiated by an advanced waveguide coupler.[20] Based on the highly peaked structure of the wave about the magnetic axis, it is likely that fast wave heating in such devices will be favorably concentrated in the central region of the discharge.

V. CONCLUSIONS

In this paper, fast magnetosonic wave propagation and focussing have been examined in a simplified tokamak model using a parabolic approximation of the wave equation. Based on fast wave field calculations over a wide range of plasma parameters appropriate for moderately sized devices such as PLT to reactor-sized devices, we conclude that power deposition is more favorably concentrated about the magnetic axis in the larger, more dense plasmas anticipated in tokamak reactors than in the plasmas currently producible in PLT.

The physical motivation for the parabolic approximation is the slow poloidal variation of the wave field relative to the radial variation over most of the plasma discharge. By treating poloidal derivative terms as perturbations and extracting the rapidly varying dominant waveform, $\varepsilon_o(r)$, from the poloidal component of the field, the coupled system of second order partial differential equations for the radial and poloidal electric fields collapses into an algebraic equation for E_r, a second order ordinary differential equation for the waveform, ε_o, and a parabolic diffusion-type equation for the remaining amplitude modulation function, $\psi(r,\theta)$. Diffractive and focussing effects are included self-consistently by this method, since continuous representations for the wave electric field components are computed directly. Hence, a more accurate representation for the wave fields is obtained than can be derived on the basis of ray tracing techniques. In addition, an algorithm based on this approach is numerically more efficient than standard ray tracing codes. Finally, absorption and mode conversion effects can be easily incorporated into this model by connecting the propagation solutions obtained in the outer regions using a cold plasma model with fully kinetic solutions obtained in the inner absorption/mode conversion

layer using a hot plasma model. This connection is being studied and will be discussed more thoroughly in future reports.

Some potentially important physical aspects of ICRF heating processes have not yet been treated adequately in the existing model. One remaining question concerns the extent to which the toroidal nature of the equilibrium influences the wave propagation and focal spot formation. In the outer propagation regions, the main complication resulting from toroidicity or noncircularity of the plasma cross section is a weak poloidal dependence in the dielectric tensor elements. It appears likely that this additional poloidal dependence can be handled using perturbation techniques. In the transition layer, the dominant toroidal effect is a variation of the dielectric tensor elements with major radius. This can easily be handled by numerically integrating a somewhat more complicated version of Eq. (35) in which the coefficients are known functions of the independent variable x. A second, more difficult problem which needs to be addressed is how to retain properly vertical phase coherence of the incident wavefront in kinetic calculations in the absorption/mode conversion layer when vertical inhomogeneities in the layer are significant. Finally, significant departure of the minority ion velocity distribution function from a Maxwellian has been observed experimentally.[21] Wave polarization calculations can be used to determine the evolution of the ion velocity space distribution function via Fokker Planck techniques. Though this effect has been considered previously by Hwang et al.[8] using a ray tracing analysis of the wave fields, the wave polarizations determined using the methods outlined in this report will include mode conversion and wave transmission effects which are ignored by the ray tracing solutions.

ACKNOWLEDGMENTS

We wish to acknowledge discussions with Dr. J.C. Hosea, Dr. D.G. Swanson, Dr. P.L. Colestock, and Dr. M.W. Phillips which helped to elucidate some aspects of the work reported here.

This work was supported by DOE Contract # DE-AC02-76-CHO-3073.

REFERENCES

1 W.M. Stacey, in U.S. FED-INTOR activity, Georgia Inst. Tech., Rep. USAFED-INTOR 82-1 (1982).

2 P.H. Rebut, in Heating in Toroidal Plasmas (Proc. 3rd Joint Varenna-Grenoble Int. Symp., Grenoble, 1982), Commission of the European Communities, Brussels, Rep. EUR-7979-EN, Vol. III, p. 989 (1982).

3 Y-K.M. Peng et al., in Plasma Physics and Controlled Nuclear Fusion Research 1982 (Proc. 9th Int. Conf., Baltimore, 1982) Vol. I, p. 409, (1982).

4 E. Mazzucato et al., in Plasma Physics and Controlled Nuclear Fusion Research 1984 (Proc. 10th Int. Conf. London, 1984) paper IAEA-CN-44/F-I-2, Vol. I, p. 433 (1985).

5 T.H. Stix, Nucl. Fusion 15, 737 (1975).

6 F.W. Perkins, Nucl. Fusion 17, 737 (1975).

7 B.D. McVey, Nucl. Fusion 19, 461 (1979).

8 D.Q. Hwang et al., Proc. Int. Conf. Plasma Physics, (Nagoya, Japan, April, 1980) p. 213 (1980).

9 V.P. Bhatnagar et al., Nucl. Fusion 24, 955 (1984).

10 I.B. Bernstein, Phys. Fluids 18, 320 (1975).

11 P.L. Colestock and R.J. Kashuba, Nucl. Fusion 23, 763 (1983).

12 D.G. Swanson, Nucl. Fusion 20, 949 (1980); Phys. Fluids 24, 2035 (1981).

13 V.A. Fock, Electromagnetic Diffraction and Propagation Problems, (Pergamon Press, NY, 1965) p. 213.

14 H.A. Haus, Waves and Fields in Optoelectronics, (Prentice-Hall, NJ, 1984), Chapter 4.

15 F. Tappert, J. Opt. Soc. Am. 66, 1368 (1976).

16 H.L. Wilson and F.D. Tappert, J. Acoust. Soc. Am. 66, 256 (1979).

17 I.M. Besieris and S.J. Patsiokas, in Proc. Southeastcon '77, (IEEE, Williamsburg, VA, April, 1977), p. 581.

18 G.B. Elder and F.W. Perkins, Jr., IEEE Trans. Plasma Sci. PS-8, 494 (1980).

19 T.H. Stix, The Theory of Plasma Waves, (McGraw-Hill, USA, 1962), Chapter 2.

20 F.W. Perkins and R.F. Kluge, IEEE Trans. Plasma Sci. PS-12, 161 (1984).

21 J. Hosea et al., Phys. Rev. Lett. 43, 1802 (1979).

Table I

	PLT	TFTR	Reactor
B_{To} (tesla)	1.9	4	4
R_o (m)	1.34	2.55	3.25
a (m)	0.40	0.83	1.3
f (MHz)	30	63	63
$n_e(o)$ (cm^{-3})	6×10^{13}	6×10^{13}	1.2×10^{14}
$n_D(o)$ (cm^{-3})	5.7×10^{13}	5.7×10^{13}	1.14×10^{14}
$n_H(o)$ (cm^{-3})	0.3×10^{13}	0.3×10^{13}	0.06×10^{14}
$N = k_{\parallel} R_o$	9	9	9
P_o (MW)	3	10	20

FIGURE CAPTIONS

Fig. 1 Geometry The plasma cross section is divided into three regions. A paraxial approximation is applied in Region I which extends from the plasma edge to the planes $x = x_o, x_1$. Mode conversion and ion cyclotron absorption effects are important in Region III, delineated by $x_{c1} < x < x_{co}$. Strong focussing and diffractive effects are treated in the transition layers, $x_1 < x < x_{c1}$ and $x_{co} < x < x_o$, which comprise Region II. Both cylindrical (r,θ,z) and Cartesian (x,y,z) coordinates are used with a common origin at the magnetic axis at R_o. The minority fundamental/majority second harmonic cyclotron resonance layer is located between $x = R_o$ and $x = x_{co}$.

Fig. 2 Density Profile The chosen density profile is constant in the central regions of the discharge, $0 \leq r \leq a/2$, and decreases parabolically for $r > a/2$ to zero at the plasma edge.

Fig. 3 Antenna Current Profile A half-turn loop antenna is simulated using a cosine distribution for the antenna current for $\theta_m \geq \theta \geq -\theta_m$.

Fig. 4 Radial Waveforms from Paraxial Solutions in Region I The real part of the lowest order approximation, $\varepsilon_o(r)$, of the poloidal electric field in the outer propagation region is shown for PLT in (a), TFTR in (b), and a reactor-sized tokamak in (c). Note that the relative ratio of radial wavelength to plasma minor radius decreases as size and density of the plasma increases.

Fig. 5 Contours of $(B_z)_{real}$ in PLT Fast wave launched from an antenna at the outside edge with a current distribution as shown in Fig. 3 with $\theta_m = 80°$ is focussed into a spot of approximate diameter equal to a/2.

Fig. 6 Contours of $(B_z)_{real}$ in TFTR Same as Fig. 5, except that the diameter of the focal spot has decreased to about a/4.

Fig. 7 Contours of $(B_z)_{real}$ in a Reactor Same as Fig. 5, except that the diameter of the focal spot has decreased to about a/8.

Fig. 8 Contours of $(B_z)_{real}$ in a Compact Ignition Device Same as Fig. 5 except that $\theta_m = 30°$ to model the fields radiated by an advanced waveguide coupler.

#85X0670

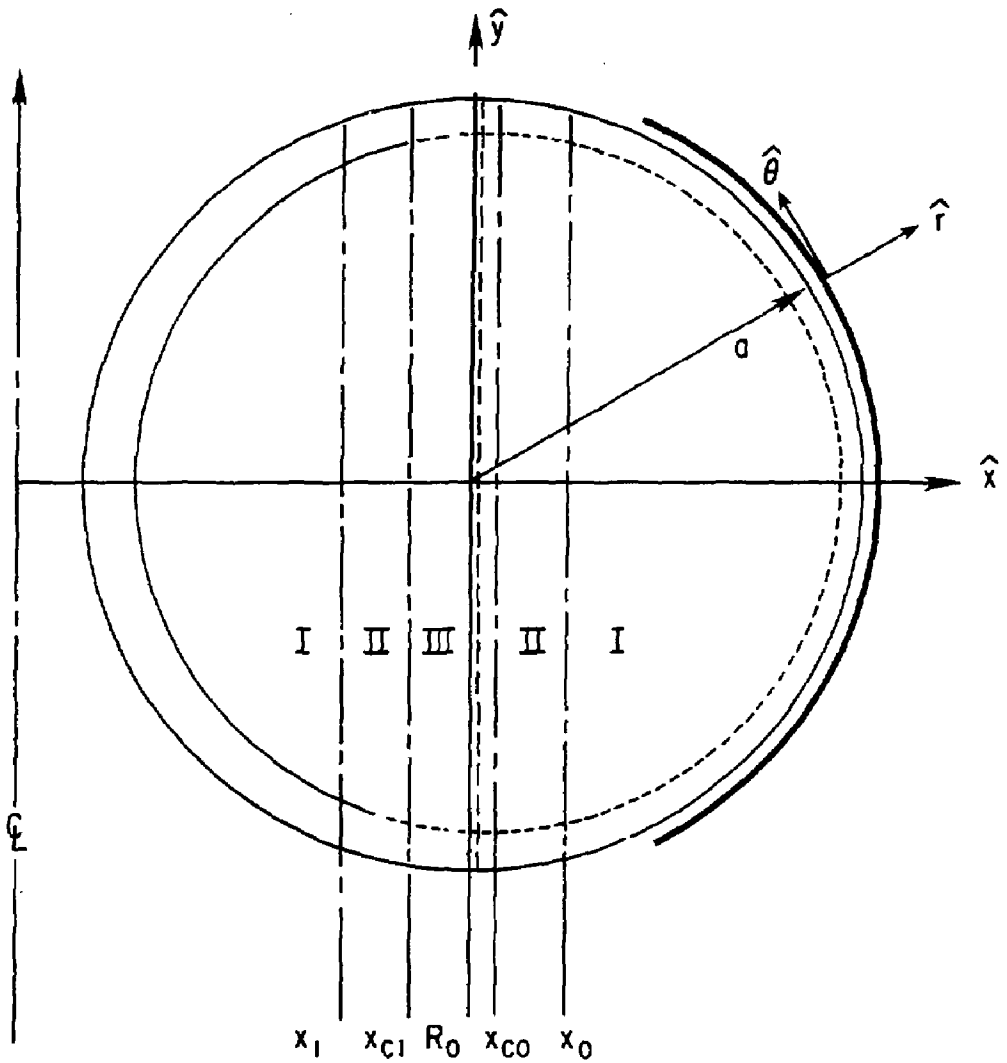

PLASMA GEOMETRY

Fig. 1a

#85X0669

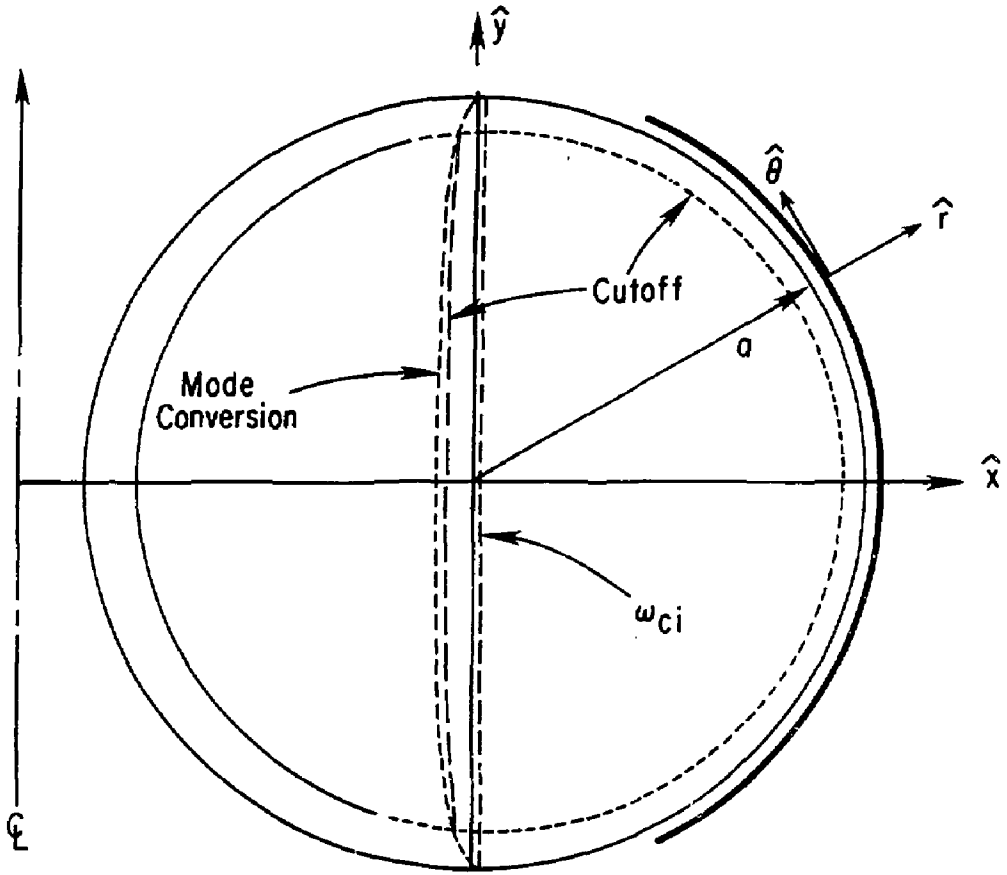

PLASMA GEOMETRY

Fig. 1b

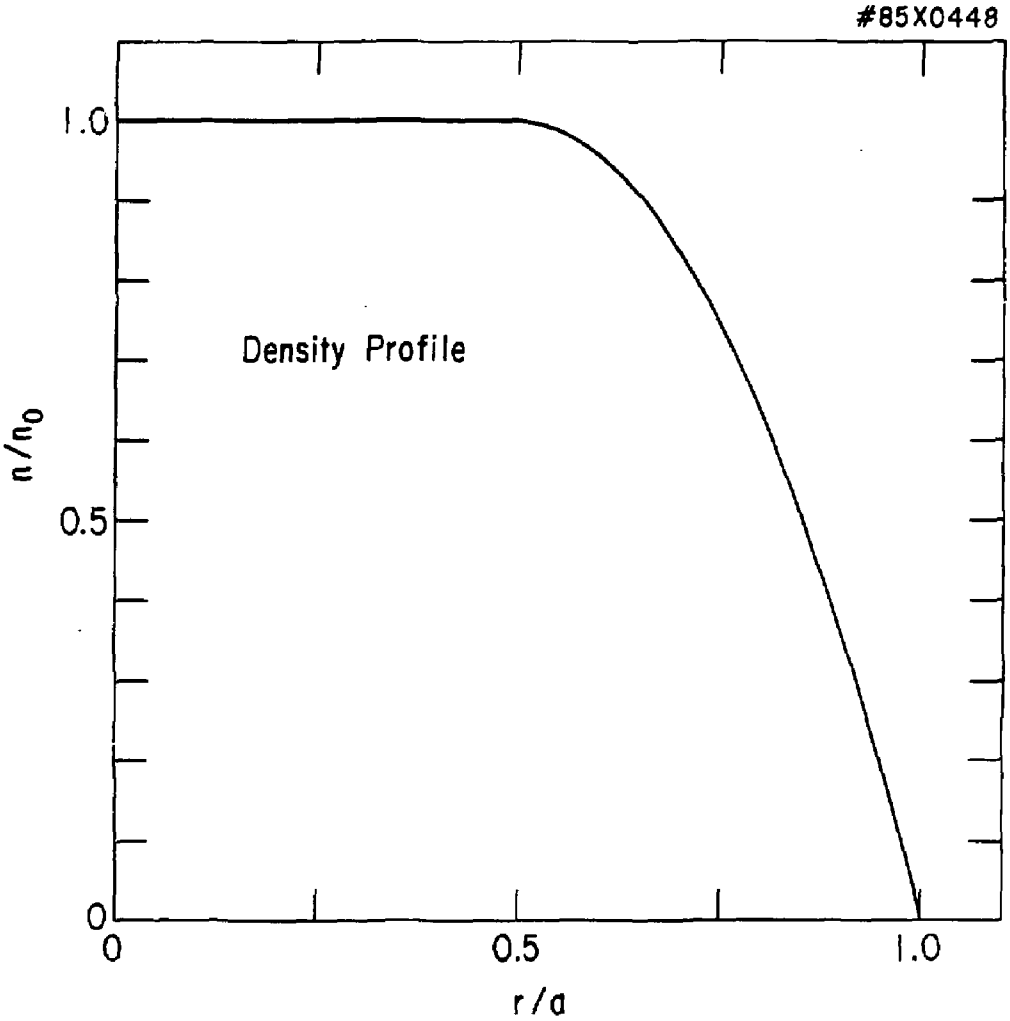

Fig. 2

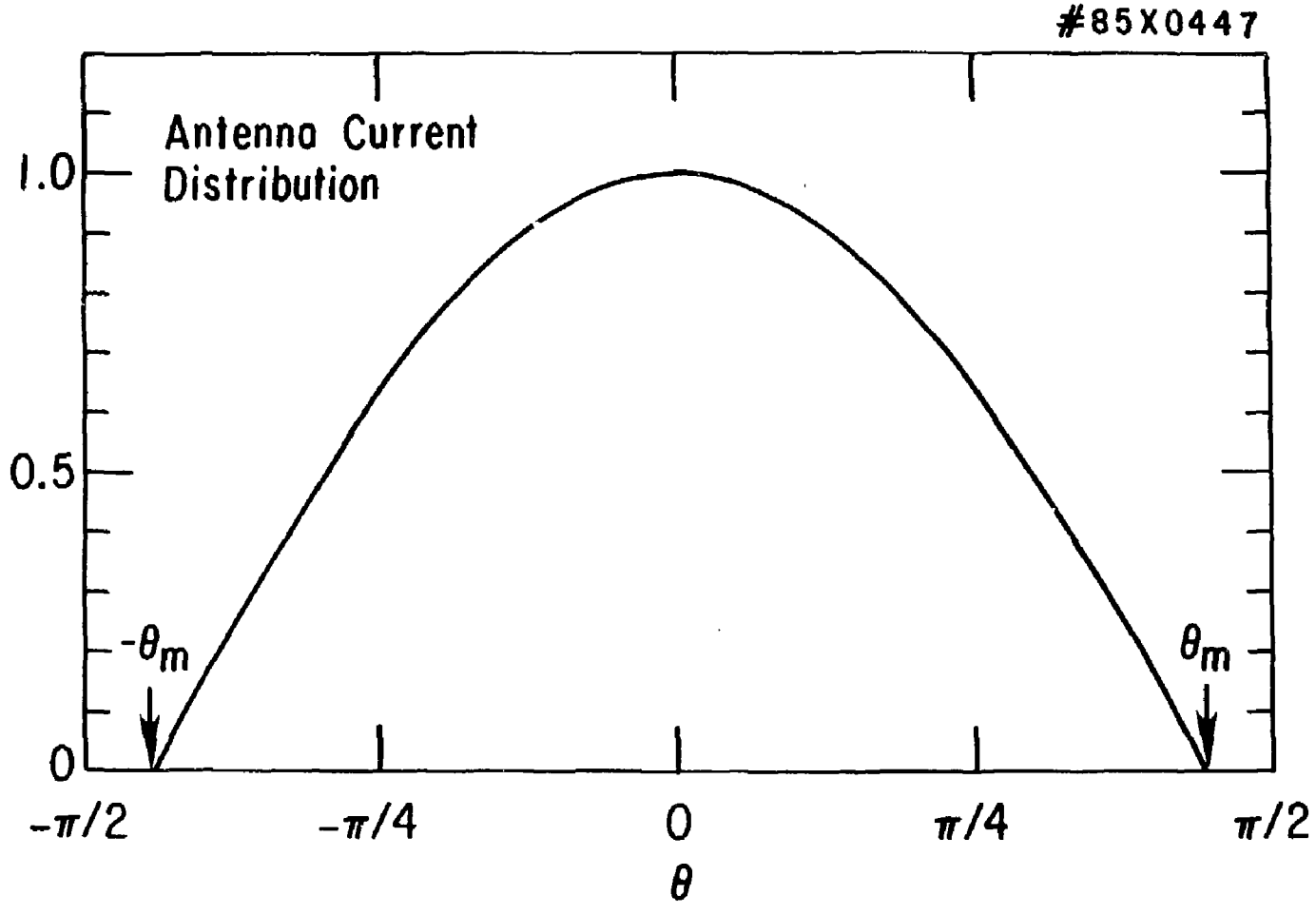
#85X0447
Antenna Current
Distribution
1.0
0.5
0
$-\theta_m$
θ_m
$-\pi/2$
$-\pi/4$
0
$\pi/4$
$\pi/2$
θ

Fig. 3

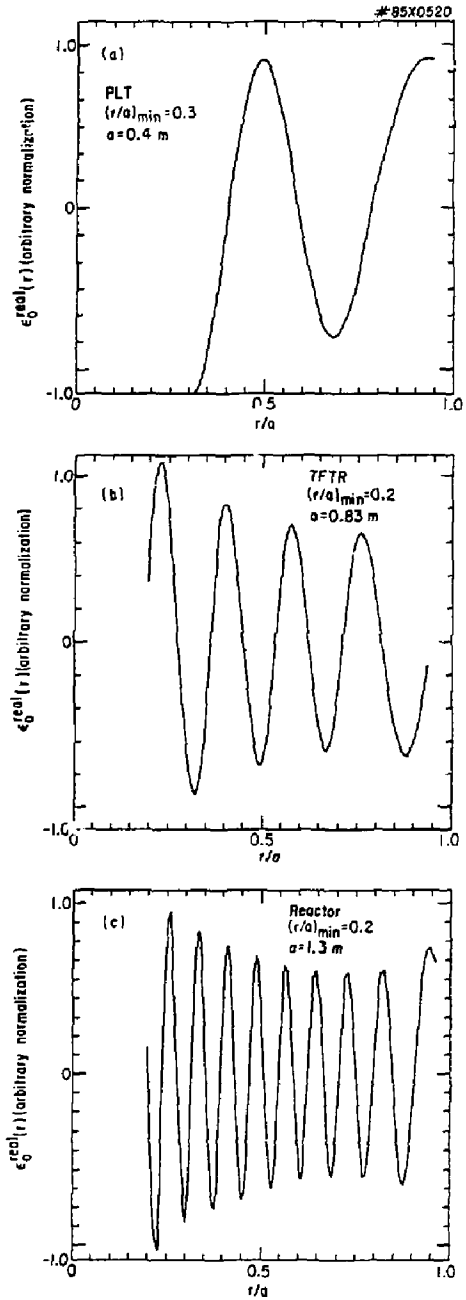
#85X0520
(a)
PLT
$(r/a)_{min}$=0.3
a=0.4 m
$\epsilon_0^{real}(r)$ (arbitrary normalization)
r/a
(b)
TFTR
$(r/a)_{min}$=0.2
a=0.83 m
$\epsilon_0^{real}(r)$ (arbitrary normalization)
r/a
(c)
Reactor
$(r/a)_{min}$=0.2
a=1.3 m
$\epsilon_0^{real}(r)$ (arbitrary normalization)
r/a

Fig. 4

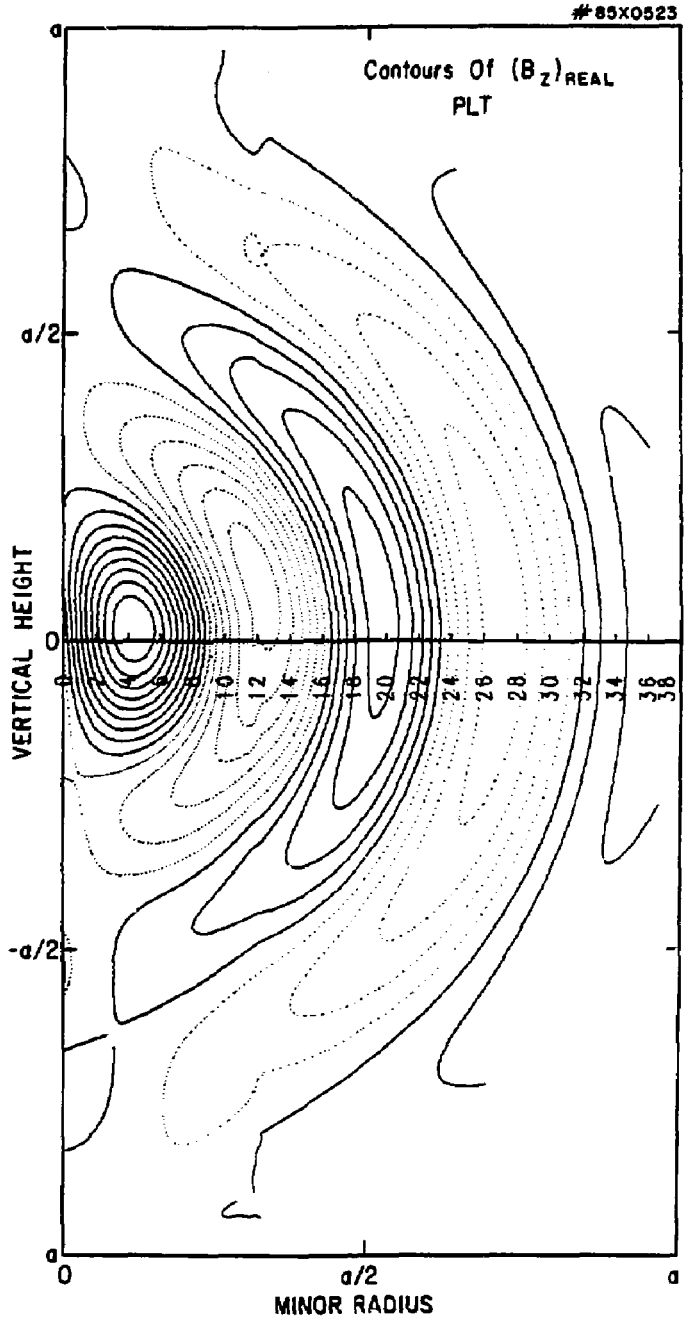
#85X0523
Contours Of $(B_z)_{REAL}$
PLT
a
a/2
0
-a/2
a
VERTICAL HEIGHT
0
a/2
a
MINOR RADIUS
0
2
4
6
8
10
12
14
16
18
20
22
24
26
28
30
32
34
36
38

Fig. 5

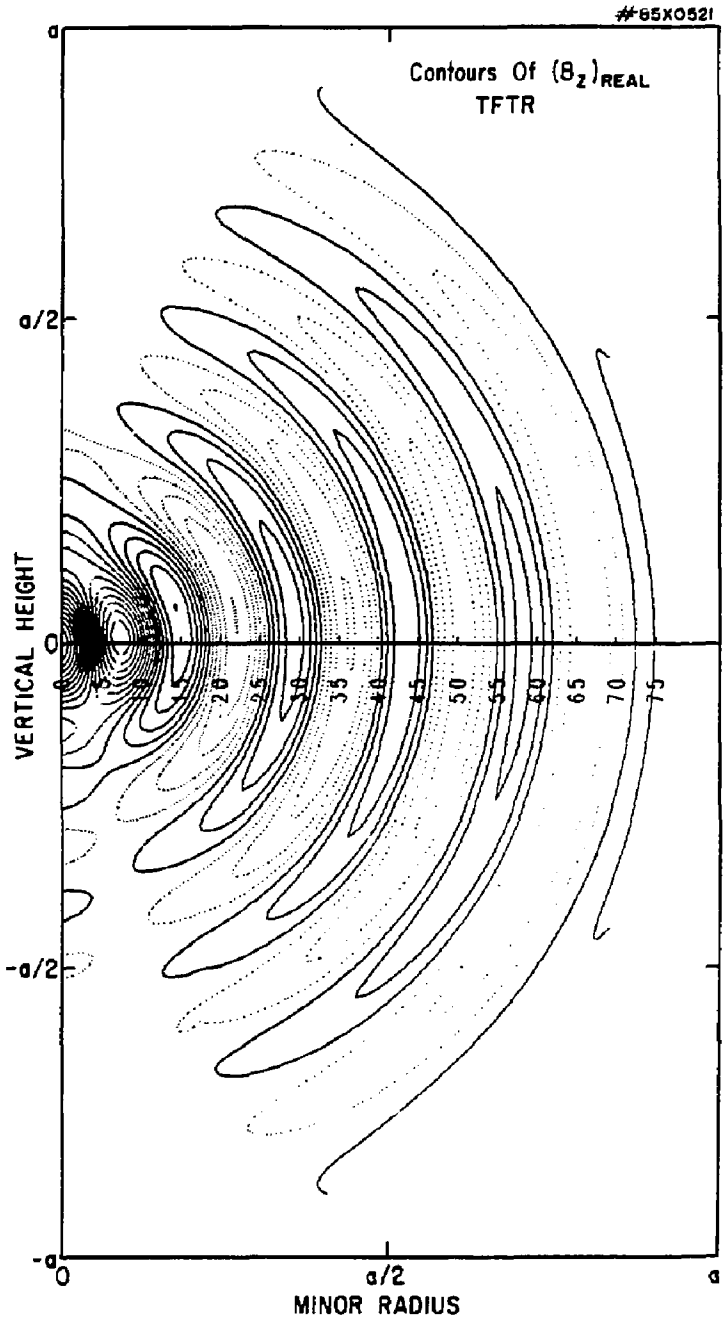
#85X0521
Contours Of $(B_z)_{REAL}$
TFTR
a
a/2
0
-a/2
-a
VERTICAL HEIGHT
0
a/2
a
MINOR RADIUS
5
10
15
20
25
30
35
40
45
50
55
60
65
70
75

Fig. 6

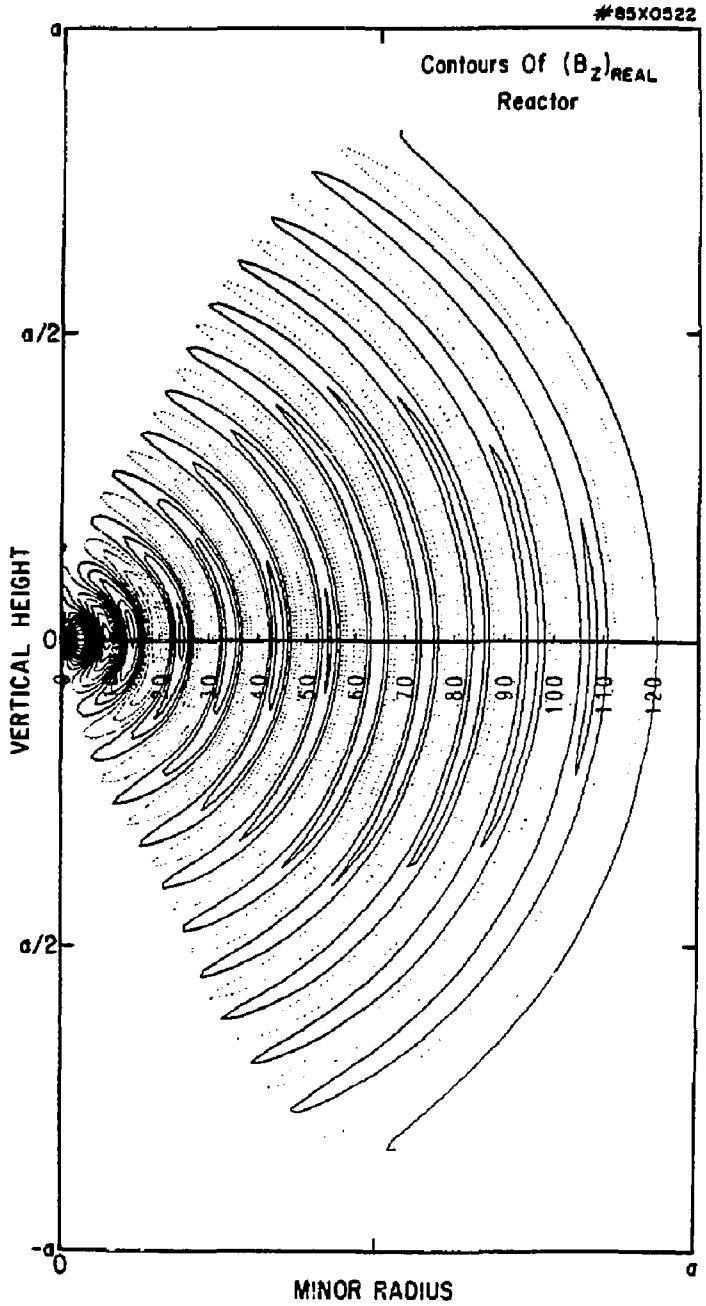
#85X0522
Contours Of $(B_Z)_{REAL}$
Reactor
a
a/2
0
a/2
-a
VERTICAL HEIGHT
0
a
MINOR RADIUS
10
20
30
40
50
60
70
80
90
100
110
120

Fig. 7

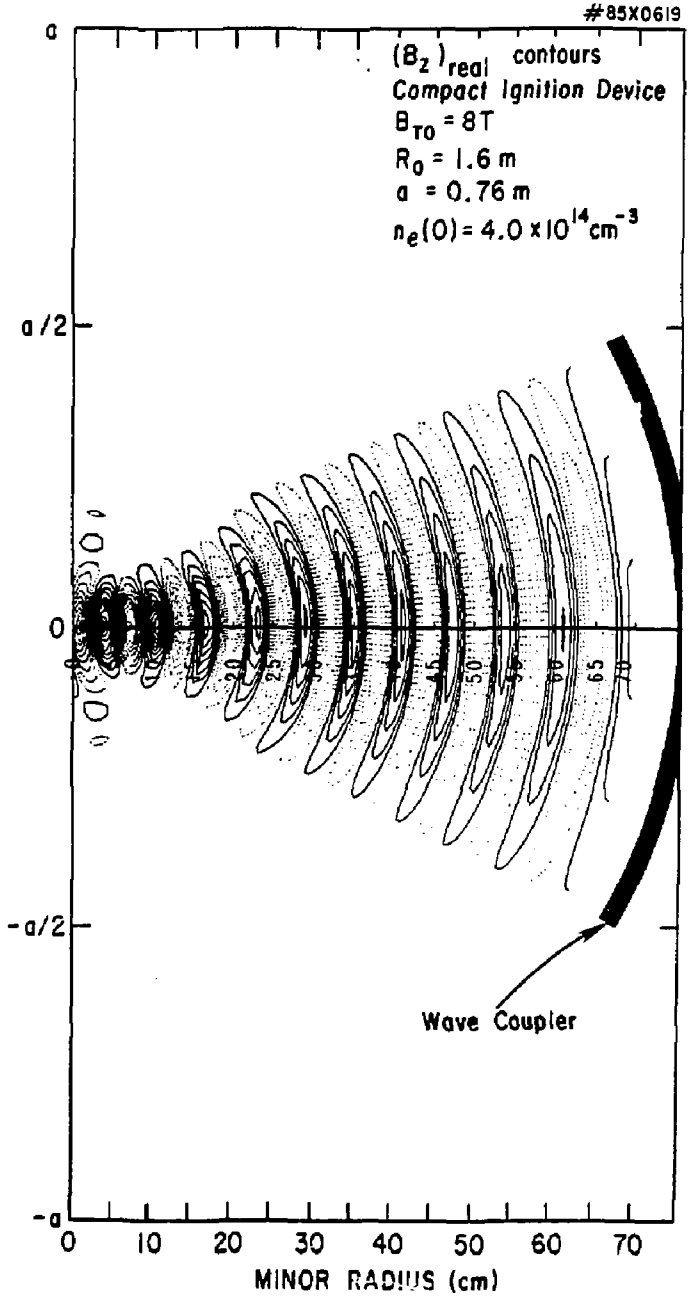
#85X0619
$(B_z)_{real}$ contours
Compact Ignition Device
$B_{T0} = 8T$
$R_0 = 1.6\ m$
$a = 0.76\ m$
$n_e(0) = 4.0 \times 10^{14} cm^{-3}$
a
a/2
0
-a/2
-a
0
10
20
30
40
50
60
70
MINOR RADIUS (cm)
Wave Coupler

Fig. 8

EXTERNAL DISTRIBUTION IN ADDITION TO UC-20

Plasma Res Lab, Austra Nat'l Univ, AUSTRALIA
Dr. Frank J. Paoloni, Univ of Wollongong, AUSTRALIA
Prof. I.R. Jones, Flinders Univ., AUSTRALIA
Prof. M.H. Brennan, Univ Sydney, AUSTRALIA
Prof. F. Cap, Inst Theo Phys, AUSTRIA
Prof. Frank Verheest, Inst theoretische, BELGIUM
Dr. D. Palumbo, Dg XII Fusion Prog, BELGIUM
Ecole Royale Militaire, Lab de Phys Plasmas, BELGIUM
Dr. P.H. Sakanaka, Univ Estadual, BRAZIL
Dr. C.R. Jahes, Univ of Alberta, CANADA
Prof. J. Teichmann, Univ of Montreal, CANADA
Dr. R.M. Skarsgard, Univ of Saskatchewan, CANADA
Prof. S.R. Sreenivasan, University of Calgary, CANADA
Prof. Tudor W. Johnston, INRS-Energie, CANADA
Dr. Hannes Barnard, Univ British Columbia, CANADA
Dr. M.P. Bachynski, MPB Technologies, Inc., CANADA
Chalk River, Nucl Lab, CANADA
Zhengwu Li, SW Inst Physics, CHINA
Library, Tsing Hua University, CHINA
Librarian, Institute of Physics, CHINA
Inst Plasma Phys, Academia Sinica, CHINA
Dr. Peter Lukac, Komenskeho Univ, CZECHOSLOVAKIA
The Librarian, Culham Laboratory, ENGLAND
Prof. Schatzman, Observatoire de Nice, FRANCE
J. Radet, CEN-BP6, FRANCE
AM Dupas Library, AM Dupas Library, FRANCE
Dr. Tom Mual, Academy Bibliographic, HONG KONG
Preprint Library, Cent Res Inst Phys, HUNGARY
Dr. S.K. Trehan, Panjab University, INDIA
Dr. Indra Mohan Lal Das, Banaras Hindu Univ, INDIA
Dr. L.K. Chavda, South Gujarat Univ, INDIA
Dr. R.K. Chhajlani, Vikram Univ. INDIA
Dr. B. Dasgupta, Saha Inst, INDIA
Dr. P. Kaw, Physical Research Lab, INDIA
Dr. Phillip Rosenau, Israel Inst Tech, ISRAEL
Prof. S. Cuperman, Tel Aviv University, ISRAEL
Prof. G. Rostagni, Univ Di Padova, ITALY
Librarian, Int'l Ctr Theo Phys, ITALY
Miss Clelia De Palo, Assoc EURATOM-ENEA, ITALY
Biblioteca, del CNR EURATOM, ITALY
Dr. H. Yamato, Toshiba Res & Dev, JAPAN
Direc. Dept. Lg. Tokamak Dev. JAERI, JAPAN
Prof. Nobuyuki Inoue, University of Tokyo, JAPAN
Research Info Center, Nagoya University, JAPAN
Prof. Kyoji Nishikawa, Univ of Hiroshima, JAPAN
Prof. Sigeru Mori, JAERI, JAPAN
Library, Kyoto University, JAPAN
Prof. Ichiro Kawakami, Nihon Univ, JAPAN
Prof. Satoshi Itoh, Kyushu University, JAPAN
Dr. D.I. Choi, Adv. Inst Sci & Tech, KOREA
Tech Info Division, KAERI, KOREA
Bibliotheek, Fom-Inst Voor Plasma, NETHERLANDS
Prof. B.S. Liley, University of Waikato, NEW ZEALAND
Prof. J.A.C. Cabral, Inst Superior Tecn, PORTUGAL
Dr. Octavian Petrus, ALI CUZA University, ROMANIA
Prof. M.A. Hellberg, University of Natal, SO AFRICA
Dr. Johan de Villiers, Plasma Physics, Nucor, SO AFRICA
Fusion Div. Library, JEN, SPAIN
Prof. Hans Wilhelmson, Chalmers Univ Tech, SWEDEN
Dr. Lennart Stenflo, University of UMEA, SWEDEN
Library, Royal Inst Tech, SWEDEN
Centre de Recherchesen, Ecole Polytech Fed, SWITZERLAND
Dr. V.T. Tolok, Kharkov Phys Tech Ins, USSR
Dr. D.D. Ryutov, Siberian Acad Sci, USSR
Dr. G.A. Eliseev, Kurchatov Institute, USSR
Dr. V.A. Glukhikh, Inst Electro-Physical, USSR
Institute Gen. Physics, USSR
Prof. T.J.M. Boyd, Univ College N Wales, WALES
Dr. K. Schindler, Ruhr Universitat, W. GERMANY
Nuclear Res Estab, Julich Ltd, W. GERMANY
Librarian, Max-Planck Institut, W. GERMANY
Bibliothek, Inst Plasmaforschung, W. GERMANY
Prof. R.K. Janev, Inst Phys, YUGOSLAVIA